Facility for Calibrating Anemometers as a Function of Air Velocity Vector and Turbulence

Iosif I. Shinder*, Michael R. Moldover, B. James Filla, Aaron N. Johnson, Vladimir B. Khromchenko
National Institute of Standards and Technology, Gaithersburg, MD 20899, USA

Abstract

NIST calibrates anemometers as a function of airspeed vector and turbulence intensity (*Tu*). The vector capability (sometimes called "3-D") is particularly important for calibrating multi-hole differential-pressure probes that are often used to quantify pollution emitted by smokestacks of coal-burning electric power plants. Starting with a conventional "1-D" wind tunnel, we achieved vector and *Tu* capabilities by installing translation/rotation stages and removable turbulence generators (grids or flags). The calibration ranges are: yaw angle ±180°; pitch angle ±45°; airspeed 1 m/s to 30 m/s; turbulence intensity $0.07 \leq Tu \leq 0.25$; average data collection rate: 300 points/hour at fixed *Tu*. The system's expanded uncertainties corresponding to 95 % confidence level are: airspeed $0.0045\times|V|+(0.036/|V|)^2$ where $|V|$ is the magnitude of the airspeed in m/s; pitch and yaw angles 0.3°; and turbulence intensity 0.03 *Tu*. The airspeed working standard is a Laser Doppler Anemometer that is traced to SI unit of velocity *via* a spinning disk. Calibrations are corrected for blockage by the instrument under test and its supports.

.

Key words

Airspeed vector calibration; blockage effect; hot wire probe; multi-hole pitot probe; turbulence correction; turbulent flow.

*Corresponding author.

E-mail address: iosif.shinder@nist.gov

Introduction: Air Velocity Calibrations

Accurate measurements of outdoor air flows and of gas flows in large conduits and stacks are needed by weather services and diverse industries (*e.g.* automotive, aircraft, wind-power, fossil-fueled electricity-generating). These large flows have spatial and temporal non-uniformities described as "swirls", "eddies", and "turbulence". Often, these complicated flows are quantified by using well-characterized anemometers to map (or "velocity profile") a cross-section of the flow and then integrating the map. To more-accurately characterize anemometers for velocity profiling, we modernized NIST's wind tunnel that had been built in 1967. This paper describes the improvements of the wind tunnel's hardware, software, and calibration capabilities.

NIST's updated air-velocity calibration system can characterize pitot tubes, multi-hole differential-pressure probes, thermal and ultrasonic anemometers, and anemometers that depend upon rotating cups, vanes, *etc*. In this report, we emphasize the calibration of multi-hole differential-pressure probes that are often used to comply with regulations limiting pollution emitted by smokestacks of coal-burning electric power plants. We expect that calibrated probes will reduce the cost of velocity-profile-based emission measurements while increasing the accuracy of the maps because the calibrations now account for the pitch (α) and yaw (β) angles that specify the probe's orientation with respect to the average flow velocity vector $\boldsymbol{V}$ and for the turbulence intensity Tu. [1] The quantity that we call "turbulence intensity" is the dimensionless ratio $Tu \equiv \langle V_x^2\rangle^{1/2}/\langle V_x\rangle$ where V_x is instantaneous velocity component measured by the laser Doppler anemometer (LDA) when the LDA is aligned with the velocity vector $\boldsymbol{V}$; "$\langle\rangle$" denotes a time average (typically 5 s) and $\langle V_x^2\rangle^{1/2}$ is the standard deviation $\sigma(V_x)$ measured by the LDA (after correcting for $\sigma(V_x)$ in the absence of turbulence) .

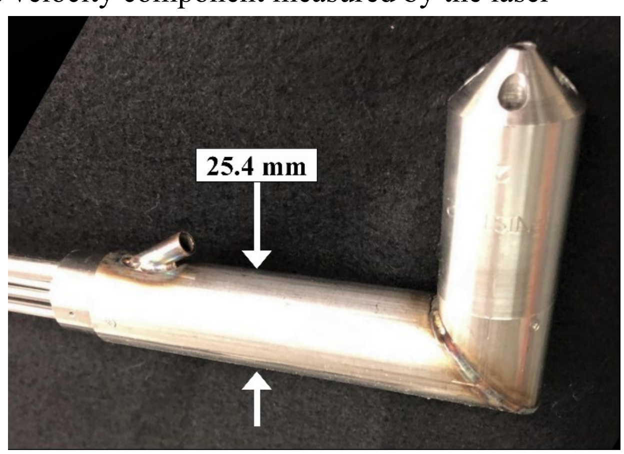

Figure 1. Multi-hole differential-pressure probe. During the probe's calibration, it was attached to a 1 m long, 25.4 mm O.D. steel support tube. The support tube enclosed narrower, pressure-transmitting tubes that connected the ports in the probe's head with differential-pressure gauges located several meters away.

Figure 1 displays an experimental multi-hole differential-pressure probe that NIST has calibrated. A *detailed* calibration of such a probe generates hundreds or thousands of values of $P_{1i}(|\boldsymbol{V}|, Tu, \alpha, \beta)$, where $P_{1i} \equiv P_1 - P_i$ is the pressure difference between port 1 and port i of the probe and $|\boldsymbol{V}|$ is the magnitude of the airspeed vector in the wind tunnel at the probe's location. For most probe geometries, $P_{1i}(|\boldsymbol{V}|, Tu, \alpha, \beta)$ is too complex to predict accurately. Complexities, particularly at large values of α or β, include excess noise and, for low values of Tu, hysteresis generated by boundary layer separation. [2] In a future publication, we will address the problem of fitting and interpolating these large calibration data sets.

NIST's updated air-velocity calibration system spans the ranges: yaw angle ±180°; pitch angle ±45°; airspeed 1 m/s to 30 m/s; turbulence intensity 0.0007 to 0.25; average data rate: 300 points/hour at fixed Tu. These specifications include the measurement ranges that are important for smokestack measurements: 5 m/s $\leq |\boldsymbol{V}| \leq$ 30 m/s and Tu on the order of 0.1. [3]

For airspeeds that NIST determines using its laser doppler anemometer (LDA), the system's expanded uncertainty[1] corresponding to 95 % confidence interval is $U_r\langle V_x\rangle = 0.004\times\langle V_x\rangle$ where $\langle V_x\rangle$ is the component of $\boldsymbol{V}$ perpendicular to LDA's interference fringes. For airspeeds that NIST determines using a calibrated pitot tube: $U_r(|\boldsymbol{V}|) = 0.0044\times|\boldsymbol{V}|+(0.013\ \mathrm{m^2/s^2}/|\boldsymbol{V}|)$. The expanded uncertainty of the pitch and yaw angles is 0.3 ° and the expanded uncertainty of the turbulence intensity measurement is $U(Tu) = 0.03\times Tu$ for $0.03 \leq Tu \leq 0.1$. There is no need to measure turbulence intensity below 0.03 since bias connected with turbulence goes as square of turbulence intensity and becomes smaller than expanded uncertainty of velocity measurement. NIST's calibrations of $P_{1i}(|\boldsymbol{V}|, Tu, \alpha, \beta)$ are traceable to the International System of Units. Such traceability is essential to earn international recognition of NIST's new capability for calibrating angle- and turbulence-dependent responses of diverse anemometers.

At the time of this writing (March 2021), 15 National Metrology Institutes (NMIs) including NIST, had posted calibration capabilities for diverse anemometers. [4] However, none of the posted capabilities consider Tu, α, and β as independent variables. Therefore, the results of any

[1] Unless otherwise stated, all uncertainties reported in this document are expanded standard uncertainties with coverage factor $k = 2$ corresponding to a 95 % confidence interval.

one these internationally-recognized calibrations can be summarized in a small table listing the anemometer's response at, perhaps, 10 to 20 different airspeeds. All the NMIs calibrate anemometers in low-turbulence air flows at ambient temperature and pressure. Prior to calibrations, those anemometers that have direction-dependent responses to the air flow are aligned with the air flow. (For example, the axis of a propeller anemometer is aligned parallel to the air stream.) In the range 0.5 m/s to 38 m/s, the smallest claimed expanded uncertainty was $|\boldsymbol{V}|) = 0.0025\times|\boldsymbol{V}|$. (Support for the claim included a comparison among 9 of the 15 NMIs. [5]) Therefore, the uncertainties claimed for the present 4-variable calibrations are only 1.6 times larger than best-in-the-world calibrations obtained under the restricted conditions: $\alpha = \beta = 0$ and $Tu \approx 0$.

The remainder of this paper is organized as follows. We describe NIST's wind tunnel and its application to the calibration of anemometers in a low-turbulence air flow. This description includes the measurements of airspeed that are traceable to primary standards of length and time as well as the translation/rotation stages that are used to support and orient anemometers during calibrations. We then discuss the generation and measurement of turbulence, followed by a description of blockage corrections and concluding with examples of calibration results and a brief comment concerning uncertainties.

2. NIST's Wind Tunnel

Figure 2 is a sketch of NIST's wind tunnel with its higher-speed test section installed. Here, we describe the tunnel's operation when turbulence generators are absent. In Section 5, we describe the changes resulting from installing turbulence generators upstream of the test section.

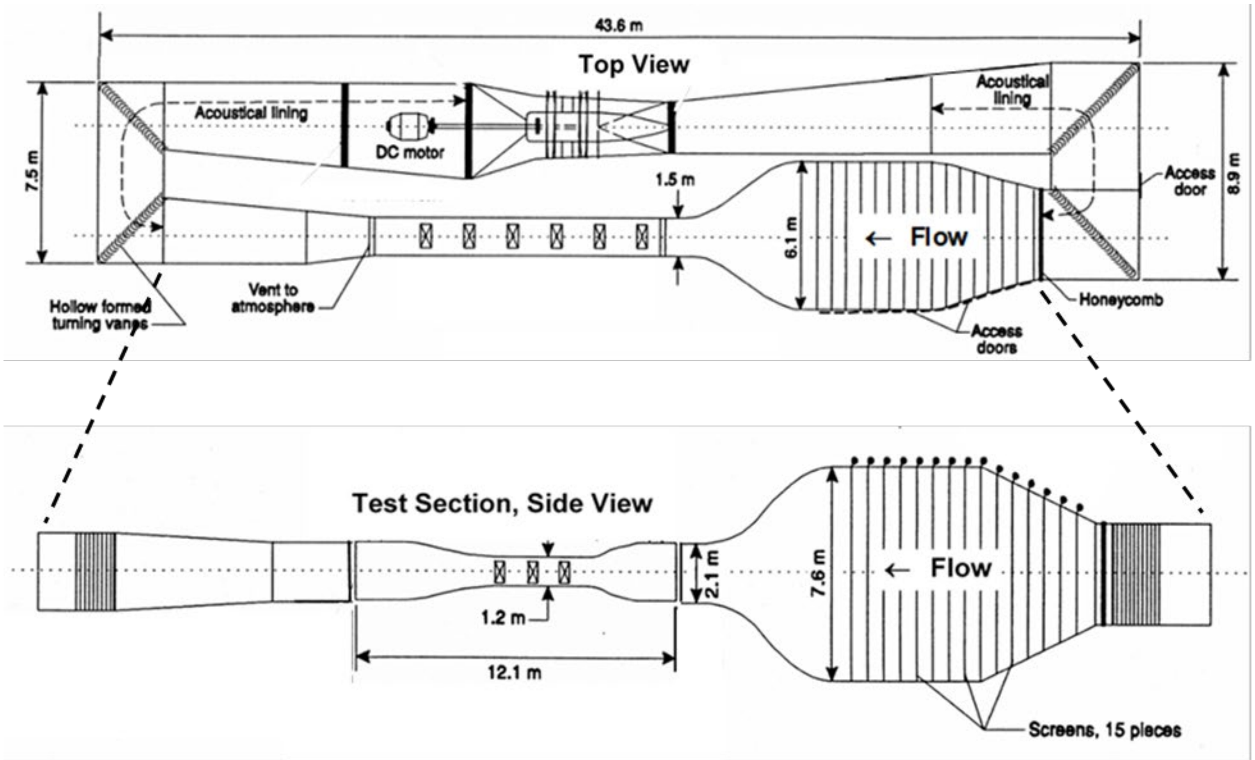

Figure 2. TOP: Top view of recirculating wind tunnel, with the low speed test section in place. BOTTOM: Expanded side view of settling chamber and high-speed test section.

As seen from above, the wind tunnel is a closed loop contained within a footprint 43.5 m long and 8.9 m wide. The fan that drives the airflow is on the opposite side of the loop from the test section that contains the working airspeed standards and any instrument under test IUT. From the fan, the airflow passes through two sets of turning vanes and into a large-cross-section, screen-filled "settling" chamber that reduces the fan-generated turbulence and swirl. The test section shown in the side view in Fig. 2 is used for calibrations spanning the range 0.15 m/s to 75 m/s. It is 12 m long and 1.5 m wide. Along the flow direction, the test section's height forms a venturi-like duct. The height gradually contracts from 2.1 m to 1.2 m. Then, it is constant for a length of 2 m. Finally, the height gradually returns to 2.1 m. In the test section, the longitudinal free-stream turbulence level is 0.001 over most of the airspeed range with a transverse airspeed gradient of less than 1 % within a working area of 90 % for all test section areas. [6] Using an LDA, we mapped the airspeed in a vertical plane that passed through the geometric center of the test section. [7] In 0.4 m wide by 0.4 m high subsection of the map, the maximum airspeed difference from the center of the test section was 0.10 % in the vertical direction and 0.15 % in the horizontal direction at the airspeed 10 m/s. Therefore, any IUT can be accurately calibrated if it is located anywhere in the subsection. If an IUT is located closer to the test section's wall during a calibration, the calibration must account for the boundary layers attached to the wind tunnel's walls.

While making the airspeed map, the airspeed was kept constant using a PID control loop linked to an L-shaped pitot tube placed on the side of the wind tunnel, as shown in Fig. 3. For normal calibrations, data are taken when the PID loop indicates that $|V|$ is controlled within the larger of 0.01 m/s or $0.002|V|$ for the range 5 m/s $\leq |V| \leq$ 40 m/s. The noise in the PID loop corresponded to air speed fluctuations of 0.01 % rms, when averaged over 50 s. We did not map the airspeed below 5 m/s because, at lower airspeeds, the uncertainty of the pitot tube measurements is larger than the uncertainty of the map. Above 20 m/s, the increasing Reynolds number increases flatness of the airspeed map in the wind tunnel's cross-section. [7]

Additional, detailed information about NIST's wind tunnel can found in [8] and [9].

3. Instruments, Coordinate System, and Positioning Stages.

Figure 3 displays the layout of the wind tunnel's test section, as viewed from above, during the calibration of a multi-hole, differential-pressure probe.

The LDA probe is permanently installed on the outside surface of the roof of the wind tunnel. When a turbulence-generating device (grid or flag array) is installed in the wind tunnel, it is located 1 m to 3.5 m upstream of the sensing volume of the LDA, depending on the turbulence intensity desired at the probe's location.

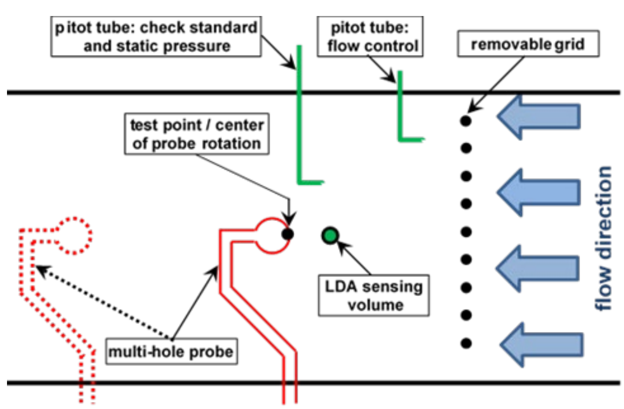

Figure 3. Schematic layout of instruments in the wind tunnel's test section, as viewed from above, when calibrating a multi-hole differential-pressure probe. The multi-hole probe is shown in two locations.

Two L-shaped pitot tubes are permanently mounted in the wind tunnel. One pitot tube serves as the airspeed sensor in a feedback loop that controls the power supply that drives the fan. It is located near the test point, but not so near that it interferes with the flow around the IUT. A second pitot tube serves as a check standard for the entire airspeed calibration system. It also monitors the static air pressure in the wind tunnel. (The static pressure is combined with data from temperature and the humidity sensors to calculate the density of the air in the wind tunnel. [8])

The test point (the leading surface of the probe being calibrated) is usually 12 cm downstream from LDA. This ensures the blockage of the flow by the IUT has only a small effect on the airspeed at the LDA. We measured the blockage by moving the probe downstream, as suggested by the dashed outline of a probe in Fig. 3 and briefly discussed in Section 7.

Figure 4 shows the two coordinate systems used during calibrations. One coordinate system is attached to the wind tunnel. Its origin is the test point which is usually located 12 cm downstream from the sensing volume of the LDA. This coordinate system is right-handed. Its *X*-axis is parallel to the wind; its *Z*-axis points up; and the *Y*-axis points to the right when looking into the wind.

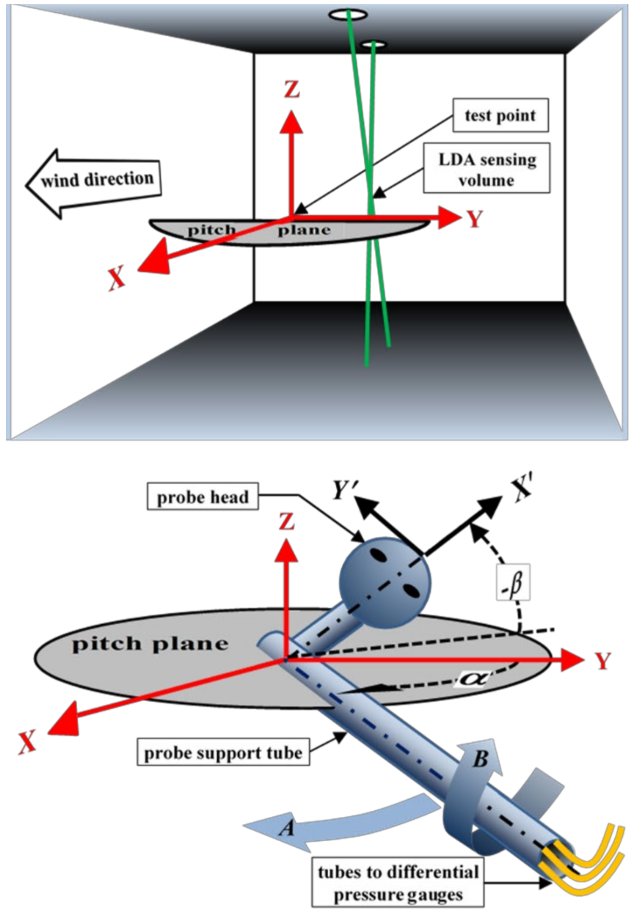

Figure 4: TOP: Wind tunnel's coordinate system. The origin of the coordinate system is the "test point" which is usually set ~12 cm downstream from the LDA's sensing volume. BOTTOM: Coordinate system for orienting a multi-hole pressure probe. The pitch angle α is in the *XY* plane. The angle α increases from zero as the probe's support tube is rotated from the *Y*-axis in the direction of the arrow "*A*". The yaw angle β specifies the orientation of the center-line of probe's head in the plane that includes both the *Z*-axis and the center-line. When the center-line is in the pitch plane, $\beta = 0$; β increases as the support tube is rotated about its axis in the direction of the arrow "*B*". The axes *X'* and *Y'* are attached to the probe being calibrated.

The second coordinate system rotates with the probe as its orientation with respect to the wind velocity changes during calibrations. Its origin is the symmetry point on the probe's head facing into the wind. Its orientation with respect to the wind velocity is specified by the pitch and yaw angles, as defined in Fig. 4. The pitch angle α is in the *XY* plane. The angle α increases from zero as the probe's support tube is rotated from the *Y*-axis in the direction of the arrow "A". The yaw angle β specifies the orientation of the probe's head in the plane that passes through both the *Z*-axis and the centerline of the probe's head. When centerline is in the pitch plane, $\beta = 0$; the angle β increases as the support tube is rotated about its axis in the direction of the arrow "*B*".

NIST routinely calibrates probes that have support tube with lengths ranging from 60 cm to 250 cm. Calibrations are conducted at user-selected pitch angles $-45° \le \alpha \le +45°$ and yaw angles $-180° \le \theta \le +180°$ with an angular resolution of 0.3°. We now describe the system that orients probes for these calibrations.

As shown in the top panel of Fig. 5, NIST uses two rotational stages on top of two translational stages to orient the IUT in the wind tunnel while maintaining the test point (12.0….0.3 cm) downstream from the sensing volume of the LDA. The translation/rotation stages are mounted on the outside wall of the wind tunnel's test section. (See photographs in Fig. 5.) The support tube of a multi-hole probe (or any other IUT) is clamped to the top stage. The support tube extends from the stages into the wind tunnel by passing through a brush that covers a slot in the test section's wall With the brush in place, the flow of laboratory air into wind tunnel has a negligible effect at the test point, as we confirmed by measurements.

Each translation and each rotation stage is driven by a servo motor. Each stage contains a manufacturer-installed absolute encoder that is read to determine the stage's position. All four servos are controlled by a deterministic PID-based master control unit, using stage position set-points calculated by the main airspeed DAC program. The stage positions are based on user requested values of pitch and yaw, or absolute stage positions. The main airspeed program then continuously collects encoder readings to confirm, and correct if necessary, the true position for each stage. During normal operation, the main program and master control unit maintains the translation stages within 0.02 mm (8 encoder steps) of their set points and the rotation stages are maintained within 0.03° (15 encoder steps).

As mentioned above, in low turbulence, the airspeed is nearly independent of location in the *YZ* plane. Therefore, the uncertainty of a calibration is not increased if the test point is displaced a few centimeters from the streamline passing through the sensing volume of the LDA. This will occur, as in the lower panel of Fig. 4 when the probe head is far from the axis of the probe support tube. When the turbulence-generating grid is in the wind tunnel, the flow through the *YZ* plane varies with the 12.7 cm periodicity of the grid. (Section 5 below) Therefore, the most accurate calibrations require the test point to remain close to the streamline from the LDA, even as the probe rotates. In a worst-case scenario (Tu = 0.1) a 2 cm uncertainty in Z will lead to a 0.5 % uncertainty in the velocity.

Figure 6 shows two possible methods of fixing the test point during a calibration in a turbulent flow. In the upper panel of Fig. 6, a carbon fiber pipe is clamped to the probe support tube and to the translation/rotation stages outside the wind tunnel. The clamp, acting as a spacer, is adjusted until test point is colinear with the carbon fiber pipe. During a calibration, the pipe rotates about its symmetry axis; however, the test point does not translate off the axis. This arrangement enables calibrations in turbulent flows of certain probes with shapes that are fixed by regulations.

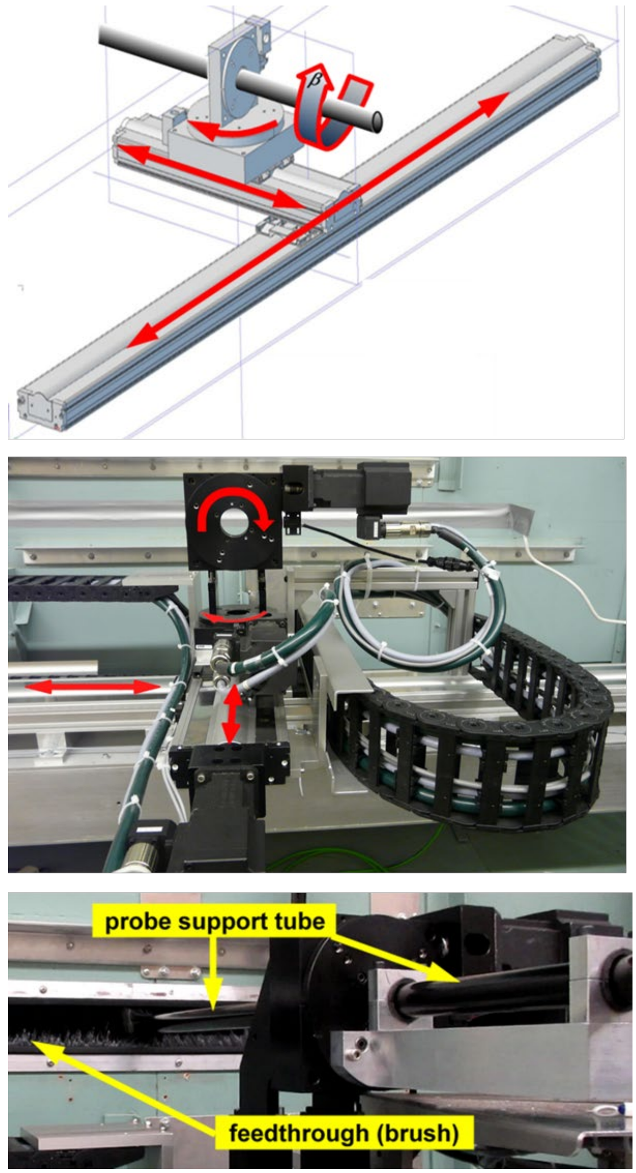

Figure 5. TOP: Schematic diagram of two translation stages and two rotation stages that orient probe-support tube at designated angles without moving the test point. MIDDLE: The rotation and translation stages are mounted on the outside of the wind tunnel's wall. BOTTOM: Probe support tube is mounted on the stages and passes through a horizontal slot in the wind tunnel's wall. The brush covering the slot reduces unwanted air flow from the laboratory into wind tunnel.

The lower panel of Fig. 6 shows a diagonal transition pipe connecting an experimental probe to a carbon fiber pipe. The dimensions of diagonal transition were chosen so that the test point was colinear with the carbon fiber pipe. Again, the test point does not translate when the carbon fiber pipe is rotated.

In response to aerodynamic forces, the test point on a typical probe is deflected much further than the tight tolerances maintained by the translation/rotation stages. We measured the motion of a test point on a carbon fiber tube by fastening a pointer to the tube's end and moving the stages until the pointer barely obstructed the LDA's sensing volume, as detected by the LDA's burst spectrum analyzer (BSA). We increased the airspeed to bend the tube and programmed the stages to return the pointer to the LDA's sensing volume. The test point's deflection was the negative of the programmed changes in the stages' positions. Near the pitch angle $\alpha = 0$, the downstream deflection was $\Delta X/\text{cm} = 0.00099\times\{\langle V_x\rangle/(\text{m/s})\}^2$ in the range 5 m/s $\leq \langle V_x\rangle/ \leq$ 30 m/s with the standard deviation $\sigma = 0.013$ cm. Under the same conditions, the tube's angular deflection was $\Delta\alpha = -0.00040°\times\{\langle V_x\rangle/(\text{m/s})\}^2$. These values of ΔX and $\Delta\alpha$ are 20 % larger than we estimated from the tube's dimensions (unsupported length L = 143 cm; O.D. = 25.4 mm; I.D. = 23.4 mm) and literature data for elastic constants and for the aerodynamic drag on a cylinder. We concluded that drag accounts for most of ΔX and $\Delta\alpha$; perhaps small contributions to ΔX and $\Delta\alpha$ result from play in the stages' bearings and deflections of the wind tunnel's walls. If a typical probe were attached to the tube, the drag might double. If so, $\Delta X \approx 1.7$ cm and $\Delta\alpha = 0.7°$

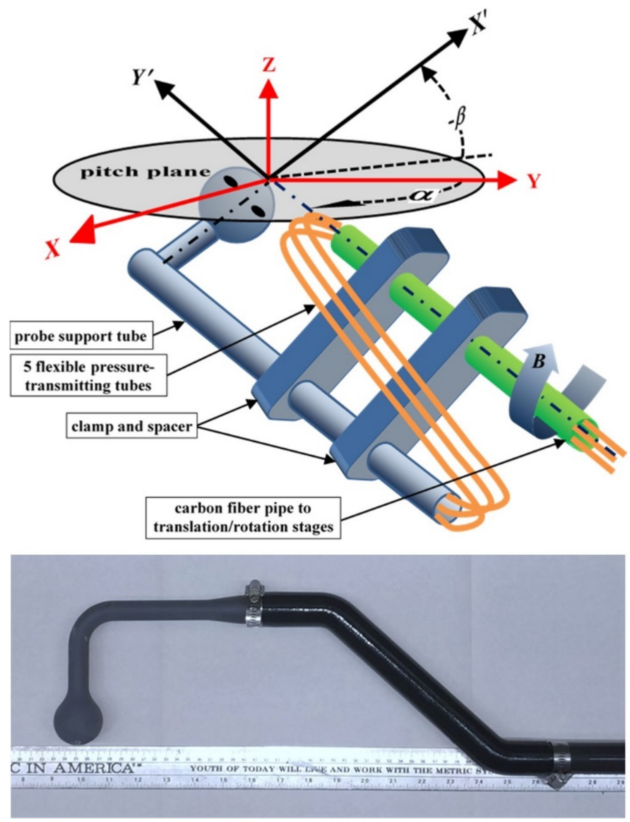

Figure 6. TOP: Coordinate systems for the wind tunnel and a probe during a calibration with turbulence. The probe's support tube is clamped to a carbon fiber pipe that leads to the translation/rotation stages outside the wind tunnel. The test point does not move when the angles α and β are changed by rotating the carbon fiber pipe about the Y' or Z axes. BOTTOM: Experimental probe connected to a carbon fiber pipe by a diagonal transition tube. By design, the diagonal transition tube ensures that the test point does not translate when the carbon fiber pipe is rotated about its axis during a calibration.

at $<V_x>$ = 30 m/s. If necessary, we can use the stages and the BSA to measure and compensate for ΔX and $\Delta\alpha$.

4. Traceable Low-Turbulence Airspeed Measurements in NIST's Wind Tunnel

References [7] and [10] provide detailed descriptions of the calibration chain linking primary standards of the International System of Units (SI) to NIST's airspeed measurements in low turbulence. Here, we briefly describe the chain. In the following Section, we describe the extension of the chain to air flows with stronger turbulence.

In low turbulence, the calibration chain starts with length and time standards that determine the diameter and rotation frequency of a spinning disk. The periphery of the disk carries a 5 μm-diameter wire that simulates tracer particles entrained in flowing air. At a well-defined, rotation-dependent speed, the wire passes through the crossed, focused laser beams comprising the sensing volume of the LDA. Some of the incident laser beam is scattered and doppler shifted by the wire and then detected by the BSA. Since 2013, NIST has used a time-consuming protocol[2] that integrates the weighted LDA velocity measurements and position of the wire over the entire sensing volume at every velocity. To conduct the integration, the LDA optical probe was mounted on an automated traverse system that moved the laser's sensing volume relative to the wire.

The response to aerodynamic forces, the same measurements established $\Delta Y = 0$ with an estimated uncertainty of less than 1 mm for pitch angles ranging from −20° to +20°. These measurements did not establish a tight bound on ΔZ because the translation/rotation stages could not change the Z coordinate. However, we expect ΔZ resulting from aerodynamic forces will be on the same order as ΔY.

[2] Reference [7] erroneously states that the newer protocol was adopted in 2011; it was adopted in 2013. In Fig. 6 of Ref. [7], the vertical axis is incorrectly labelled "(LDA speed)/(disk speed). The correct label is "(disk speed)/(LDA speed)" as appears in Fig. 7 of this work.

As discussed in [7], when LDA is correctly aligned and the spinning disk is operating correctly, a plot of LDA-indicated velocity as a function of position has a well-defined rectangular shape that has no irregularities in the sensing volume. If the sensing volume has small departures from symmetry, the calibration results may be irregular. Poorly aligned LDA beams can generate sensing volumes that contain major defects such as asymmetry or non-parallel interference fringes. If such defects are present, attempts to align the spinning disk and the LDA may produce erratic, unrepeatable, and puzzling results such as changes in the sign of the derivative of the LDA reading with respect to sensing volume position [11].

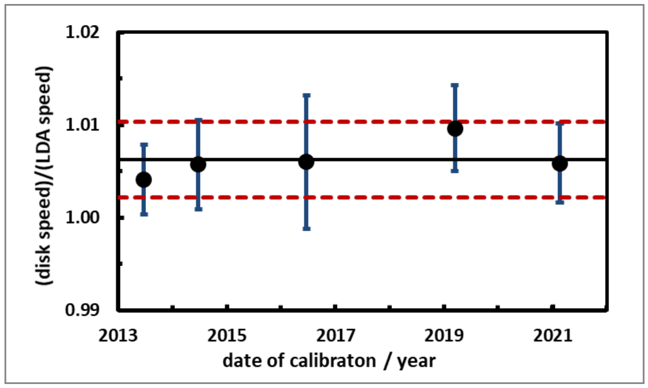

Figure 7. Control chart for calibrations of LDA using the spinning disk standard. The $k = 2$, Type A, uncertainty of each calibration is indicated by a vertical bar. The solid horizontal line at 1.0051 is the unweighted average of the four calibrations plotted. The dashed lines bracket the $k = 2$ uncertainty 0.41 %.

The ratio (disk speed)/(LDA speed) is independent of the airspeed in the range 0.2 m/s to 30 m/s within the $k = 2$ expanded relative uncertainty U_r(ratio) = 0.0041. This value of U_r(ratio) comes from Table 1 of Ref. [8].

NIST seeds the wind tunnel with droplets of di-ethyl-hexyl-sebacate (DEHS, CAS# 122-62-3). When droplets pass through the sensing volume of the LDA, they scatter and doppler-shift the laser light. The mean droplet diameter is 1.1 μm with a standard deviation of 0.1 μm. The droplets are small enough that their velocity approaches that of the air flow with a time constant on the order of 2 μs. NIST generates the droplets using an atomizer PivPart45-M series, manufactured by the PIVTEC[3] Company, Germany. Details concerning droplet generation can be found in [12]. Depending on velocity LDA data rate is in the range 1-2 kHz.

[3] In order to describe materials and procedures adequately, it is occasionally necessary to identify commercial products by manufacturer's name or label. In no instance does such identification imply endorsement by the National Institute of Standards and Technology, nor does it imply that the particular product or equipment is necessarily the best available for the purpose.

Figure 7 demonstrates the long-term stability of the LDA calibration relative to the spinning disk standard. Earlier LDA calibration data, spanning the years 1997 to 2013, are consistent with Fig. 7, albeit with larger uncertainties. We reduced the uncertainties by improving: (1) speed controls for the fan and the spinning disk, (2) generation of the oil droplets entrained in the air flow, and (3) the protocol for integrating over the LDA's sensing volume. To re-calibrate the LDA in 2021, we replaced the spinning disk described in [7] with an optical chopper, as suggested by [13]. The chopper enabled us to calibrate the LDA while it was installed on the roof of the wind tunnel. This change saved time and eliminated possible calibration changes that might occur as the LDA was removed and reinstalled on the roof of the wind tunnel.

We recall that the LDA measures only the component of the air velocity vector that is perpendicular to the surfaces of the interference fringes generated where the laser beams intersect in an ellipsoidal "sensing" volume. When the LDA was installed on the roof of the wind tunnel, it was aligned so that the surfaces of the interference fringes were parallel (±0.5°) to the *YZ* plane of the wind tunnel. With this orientation, the LDA measures the downstream (*X*) component of the air velocity incident on the IUT. The downstream component of the velocity is exactly what is required to map gas flows in smokestacks using multi-hole differential-pressure probes.

NIST's LDA uses a solid-state laser with a wavelength of 513.5 nm. The output lens of the LDA has a focal length of 1200 mm and the laser beams intersect at the angle 3.46°. The LDA's sensing volume extended 13 mm along the *Z* axis and 0.39 mm along the *X* and *Y* axes. (The sensing volume's dimensions are weakly dependent on the settings of the burst spectrum analyzer and the laser's intensity.)

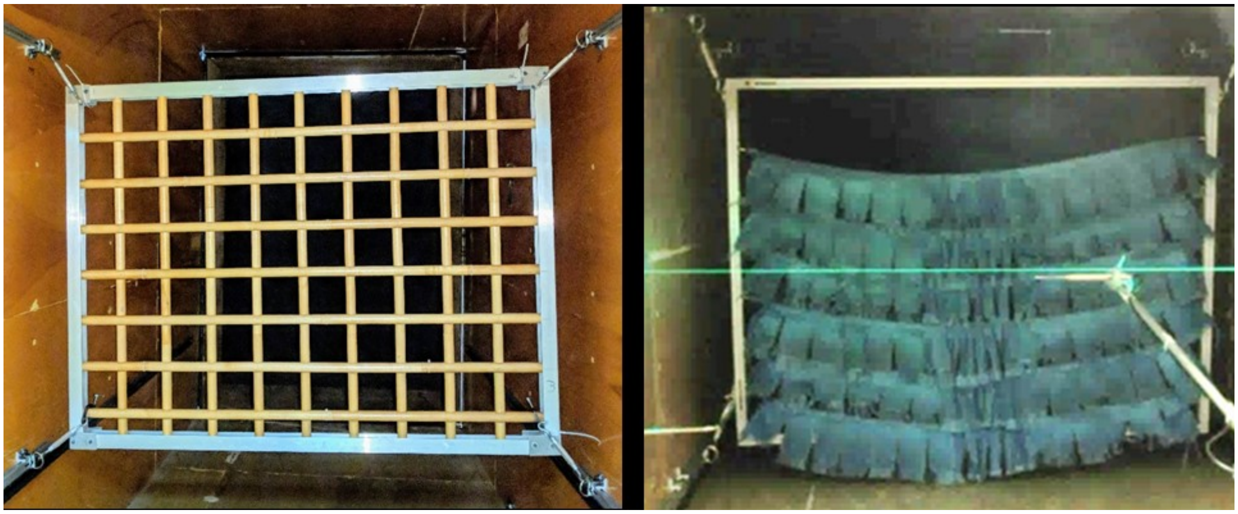

Figure 8. LEFT: Removable turbulence-generating wooden grid installed in NIST's wind tunnel. The wooden cylinders have diameters of 2.54 cm and are spaced 12.7 cm between centers. RIGHT: Removable turbulence-generating "flag" array in the wind tunnel. The flags were sewn onto ropes that are tied to a frame 1.25 m wide and 0.95 m high. (An L-shaped pitot tube and the green light from the LDA are visible downstream from the flags.)

5. Generating Turbulence

We required an economical method of generating turbulence that did not reduce NIST's ability to conduct accurate, low-turbulence measurements. We adopted Simmons and Salter's idea of generating turbulence by placing grids across the flow a wind tunnel [14]. (See [15,16,17] for recent discussions.) A theory of grid-generated turbulence was developed by Taylor in 1935. [18] Grids generate nearly homogeneous turbulence with eddies no larger than the elements of the grid; therefore, the length scale of the generated turbulence increases with the size of the grid.

We assembled the grid shown in Fig. 8 (left) using 25 mm diameter wooden cylinders arranged to form square openings 10 cm on a side. We installed permanent anchors in the walls of the wind tunnel to support the grid at well-defined locations. During normal, turbulence-dependent calibrations, these locations were upstream of the test point at the coordinates: $X = -1.06$ m, -2.00 m, or -3.56 m where the corresponding values of the turbulence intensity were Tu = 0.094, 0.056, or 0.028.

Figure 9 shows that the grid forces the X-component of the flow velocity to have a periodic Y-dependence that exceeds 1 % of V_x, even 159 cm downstream from the grid. (We did not measure the Z-dependence of V_x; we expect it has a similar periodicity.) To minimize the effects of this dependence, we used the hardware shown in Fig. 6 to fix the Y- and Z-coordinates of the test point and we took data only when $X \geq 60$ cm. Figure 10 displays the X- and Y-dependences of Tu measured using a multi-hole probe and with the grid located at the indicated distances upstream of the test point. Immediately downstream of the grid, the values of Tu in planes perpendicular to the flow have the periodicity of the grid. In these planes, Tu maxima occur where $\langle V_x \rangle$ have minima, *i.e.* in the "wake" of the grid's cylinders. The periodicity attenuates as the X (downstream) coordinate increases. As evident in Fig. 10, when $X > \approx 60$ cm, the periodicity is smaller than the noise of the Tu measurements. (In this range, the standard deviation of Tu measurements is 0.046 Tu, as indicated by the dashed lines in Fig. 10.)

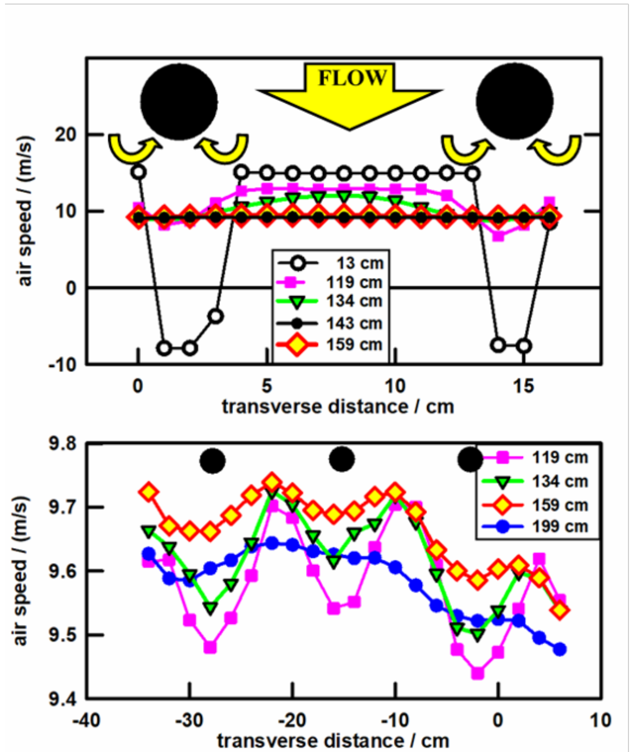

Figure 9. Flow velocity as a function of the *Y* coordinate at fixed distances downstream from the turbulence-generating grid. The black circles indicate the *Y* coordinates of the grid's vertical cylinders. The average airspeed was 9.6 m/s. However, negative (upstream) airspeeds were measured near the vertical cylinders on the 13 cm traverse, as suggested by the arrows on the upper panel.

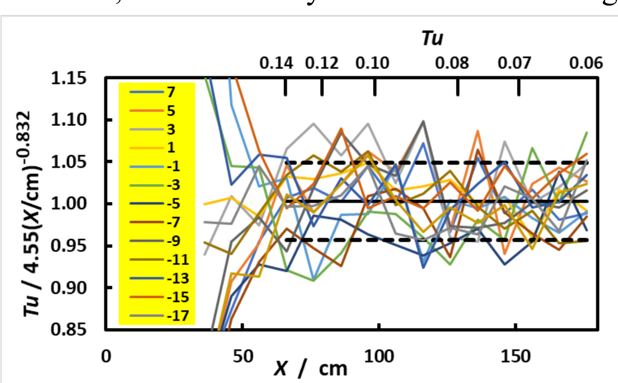

Figure 10. Measurements of turbulence intensity *Tu vs* distance *X* downstream from the grid at airspeed 10 m/s. Data span cross-stream distances: $-17 \leq Y/\mathrm{cm} \leq 7$. The dashed horizontal lines at (1.004±0.046) *Tu* indicate the standard deviations of the data from the formula $Tu = 4.55(X/\mathrm{cm})^{-0.832}$ in the range: $66 \leq X/\mathrm{cm} \leq 176$. The upper horizontal *Tu* scale indicates that the values of *X* corresponding to $0.06 \leq Tu \leq 0.14$.

When $X > \approx 60$ cm, Tu is a function of X alone: $Tu = 4.55(X/\mathrm{cm})^{-0.832}$ in the range $66 \leq X/\mathrm{cm} \leq 176$, which corresponds to $0.06 \leq Tu \leq 0.14$.

On the rare occasions when calibrations are desired at intensities greater than 0.14, the grid was replaced with an array of "flags" on a frame that was easily installed and removed from the wind tunnel. (See Fig. 8, right.) Each flag had been sewn around a rope that was tied to a frame. At airspeeds below 3 m/s, the flags moved only slightly and generated little turbulence. At airspeeds near 5 m/s, the flags generated turbulence with a wide frequency spectrum and with superimposed peaks near 5 Hz and its harmonics. [9] Above 5 Hz, the peaks moved to higher frequencies and became less prominent. The spectrum of turbulence generated by a single flag is discussed in [19, 20]. We are not aware of a publication describing the spectrum generated by an array of flags.

At airspeeds above 15 m/s, the flags began to fray. To stabilize the flags, we “trained” the assembled flag array for approximately 30 min at 25 m/s. After the training, turbulence intensity measured 50 cm downstream from the array was stable with the value $Tu = 0.20$ in airspeeds ranging from 5 m/s to 35 m/s. The training was satisfactory for 50 hours; we do not know if new problems will appear in the future.

We note that Larssen and Devenport developed an active grid that generated nearly-homogeneous turbulence with intensities $Tu \leq 0.20$ and with a flat mean-velocity profile. [21] The active grid had rhombus-shaped vanes mounted on rods that were randomly rotated by servo motors. If such an active generator were available, it might replace both the grid and the flags in Fig. 8, thereby simplifying calibrations that span a wide range of turbulence.

6. Measuring Turbulence

We tested four methods of measuring turbulence intensity: (1) Laser Doppler anemometer, (2) high-frequency, 3-D, multi-hole pressure probe with integrated pressure sensors[4], (3), constant-temperature hot-wire, anemometer and (4) an L-shaped pitot tube. As shown in Fig. 11, methods (1), (2), and (3) were in mutual agreement (within the bounds $\pm 0.10\ Tu$) in the range $0.02 \le Tu \le 0.20$ and airspeeds from 5 m/s to 25 m/s. In contrast, the turbulence intensity ratios determined with the L-shaped pitot tube were only a fraction ($0.19\ Tu_{\mathrm{LDA}}$ to $0.37\ Tu_{\mathrm{LDA}}$) of the values determined methods (1), (2), and (3). We did not study the origin of this difference; we speculate that the high-frequency pressure fluctuations at the pitot tube's port were attenuated by the response time of the differential-pressure gauge and by the time constant associated with flow in the tube connecting the differential pressure gauge to the pitot tube. If this is correct, the pitot tube can be calibrated to measure turbulence intensity, *provided that* the both the calibrator and the end user always use the pitot tube with the same pressure transducer and the same connecting tubes.

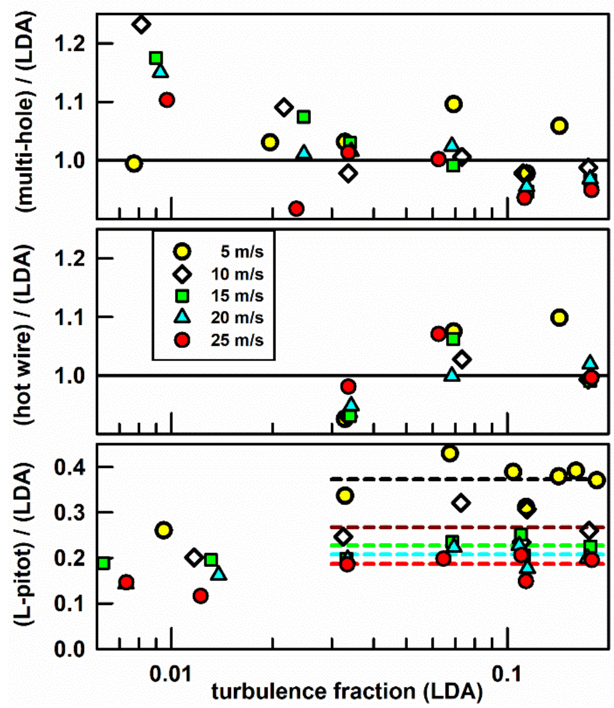

Figure 11. Turbulence intensities Tu measured with 4 instruments. The intensity ratios $Tu_{\text{multi-hole}}/Tu_{\mathrm{LDA}}$ and $Tu_{\text{hot-wire}}/Tu_{\mathrm{LDA}}$ are near 1.0, independent of airspeed and turbulence fraction. The ratios $Tu_{\text{L-pitot}}/Tu_{\mathrm{LDA}}$ range from 0.19 to 0.37 (dashed lines), depending on airspeed.

To determine Tu and its standard uncertainty $u(Tu)$ from the LDA, we recorded the data from the burst spectrum analyzer and computed the average value of the X-component of the velocity $\langle V_x \rangle$ and its relative standard deviation $\sigma_{Vx} \equiv \langle V_x^2 \rangle^{1/2} / \langle V_x \rangle$. It is an excellent approximation to replace $\langle V_x \rangle$ with $\langle V \rangle$ because $\langle V_x \rangle >> \langle V_y \rangle$ and $\langle V_x \rangle >> \langle V_z \rangle$. We assume that σ_{Vx} has two, uncorrelated sources: (1) background velocity fluctuations with the relative standard deviation $\sigma_{Vx,\mathrm{bg}}$ that are always present, even in the absence of turbulence-generating grids, and (2) grid-generated

---

[4]Integrated pressure sensors avoid the attenuation and phase delays that affect the readings of external pressure sensors that are connected to the probe by tubes.

fluctuations with the relative standard deviation $\sigma_{V\mathrm{x,grid}}$. (The background fluctuations occur because the spacing of the interference fringes generated by the LDA varies by approximately ±3 % across the sensing volume and because the tracer oil droplets pass through the sensing volume at random values of the *Y*- and *Z*-coordinates.) This widening of LDA signal does not depend on turbulence since it is inherently property of LDA. The grid-generated turbulence is isotropic; therefore, we will simplify the notation by replacing $\sigma_{V\mathrm{x,bg}}$ and $\sigma_{V\mathrm{x,grid}}$ with σ_{bg} and σ_{grid}. We computed the turbulence intensity Tu from each burst spectrum by subtracting the background velocity fluctuations from the velocity fluctuations when the grid was present:

$$Tu = \sqrt{\sigma_{\mathrm{grid}}^2 - \sigma_{\mathrm{bg}}^2} \qquad .$$

To determine the statistical contribution to the standard uncertainty $u(Tu)$ we must measure Tu many times and characterize its fluctuations. This leads us to determine the standard deviation of Tu (itself a relative standard deviation) from a sequence of burst spectra using:

$$u(Tu) = \sqrt{\sigma_{\mathrm{grid}}^2 \left(\sigma(\sigma_{\mathrm{grid}})\right)^2 + \sigma_{\mathrm{bg}}^2 \left(\sigma(\sigma_{\mathrm{bg}})\right)^2}$$

When the turbulence-generating grid was placed at three locations upstream of the test point (X = −3.56 m, −2.00 m, − 1.06 m) the turbulence intensities and their expanded uncertainties were $Tu \pm U(Tu)$ = 0.0258±0.0026, 0.0532±0.0032, 0.0950±0.0051, respectively.

7. Blockage Corrections to LDA Measurements.

To calibrate probes, NIST strives to measure the probe's response to a uniform flow in the X-direction as a function of $\langle V_x \rangle$, Tu, α, and β. The widely-used, uniform-flow convention is appropriate for mapping the flow in cross-sections of power-plant stacks with diameters that are much larger than the dimensions of the probe and its supports. In the absence of grid-generated turbulence, NIST's wind tunnel generates an excellent approximation to a uniform flow field. ($\Delta\langle V_x \rangle / \langle V_x \rangle < 0.002$ over an area of 0.4 m × 0.4 m in the Y-Z plane. [7].) However, the uniformity of the flow field is destroyed when any bluff object (such as pressure probe undergoing calibration) is inserted into the flow. For an accurate calibration, the probe must be "distant" from the sensing volume of the LDA that determines $\langle V_x \rangle$. Alternatively, the LDA-determined values of $\langle V_x \rangle$ must be corrected to account for probe-generated non-uniformity in the flow field. This correction is called a "LDA sensing volume blockage correction". [**Error! Bookmark not defined.**] This blockage correction is independent of the boundary layers separating the walls of the wind tunnel from the average flow in the tunnel.

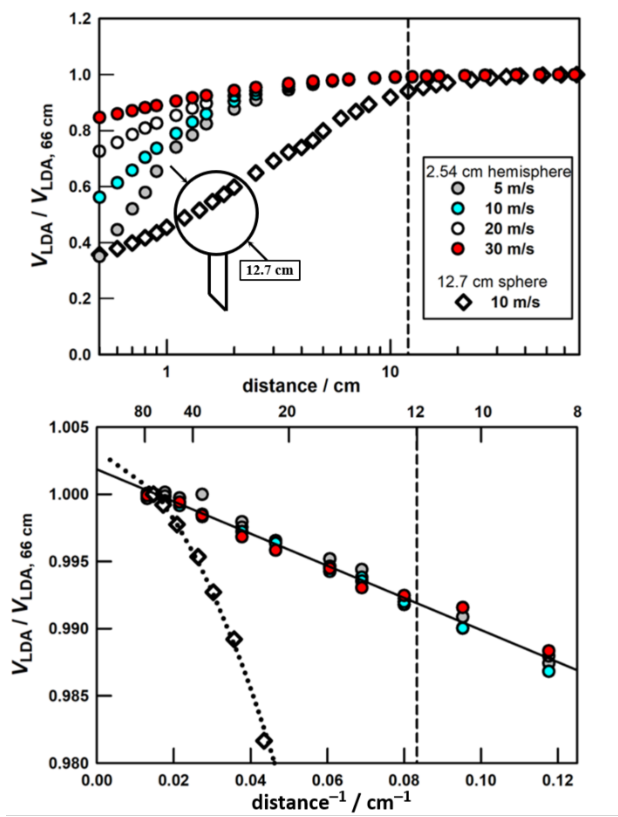

Figure 12: Top: Measured airspeed as a function of two probes' distances downstream from the LDA. Bottom: Subset of data from top as a function of inverse distance. The dotted curve and solid line show extrapolations to infinite distance. The vertical dashed lines at 12 cm indicate the position of a typical probe during a calibration.

Figure 12 displays measurements of the blockage effect for two test objects: (1) a 2.54 cm diameter, hemispherical differential-pressure probe and (2) a 12.7 cm diameter sphere. Each of these objects was mounted on a carbon fiber tube (2.54 cm diameter) that extended from the center of the wind tunnel to the translation-rotation stages outside the tunnel. To vary the blockage, the tube was translated in the X-direction, as indicated by the dashed outline in Fig. 3. During these measurements, the wind tunnel did not contain turbulence-generating structures and the air speed was maintained near 10 m/s.

The upper panel of Fig. 12 is a plot of the ratio of two LDA-determined velocities V_{LDA} / $V_{\mathrm{LDA,\,66\,cm}}$ as a function of the distance measured on a streamline between the sensing volume of the LDA and the spherical surface of the test object. (The subscript "66 cm" indicates V_{LDA} measured 66 cm upstream from the test object.) The legend of Fig. 12 identifies the data sets by their free-stream velocity $V_{\mathrm{LDA},\,\infty}$. At small distances from the hemispherical probe, V_{LDA} / $V_{\mathrm{LDA,\,66\,cm}}$ has a strong dependence on $V_{\mathrm{LDA},\,\infty}$. The dependence on $V_{\mathrm{LDA},\,\infty}$ attenuates with increasing distance as emphasized in the lower panel of Fig. 12. The lower panel of Fig. 12 expands the vertical scale of the upper panel by a factor of 80 and replaces the horizonal axis by the reciprocal of the distance. The reciprocal-distance facilitates extrapolating the data to determine $V_{\mathrm{LDA},\,\infty}$. For flows ranging from 5 m/s to 30 m/s and at distances greater than 8 cm, the data for the hemispherical probe are independent of $V_{\mathrm{LDA},\,\infty}$ and they are consistent with the linear function: $V_{\mathrm{LDA}}/V_{\mathrm{LDA,\,66\,cm}} = 1.0019 - 0.120\times(\mathrm{distance/cm})^{-1}$.

Figure 12 shows that, at 10 m/s, blockage effects for the 12.7 cm diameter sphere are much larger than those for the 2.54 cm probe and they are consistent with the empirical function: V_{LDA} / $V_{\mathrm{LDA,\,66\,cm}} = 1.003 - 7.1\times(\mathrm{distance/cm})^{-1.87}$.

When a turbulence-generating grid is present in NIST's wind tunnel, $\langle V_{\mathrm{x}}\rangle$ in most of the *Y-Z* plane has the periodicity of the grid. (Near the walls of the wind tunnel, $\langle V_{\mathrm{x}}\rangle$ has additional significant variation.) Therefore, calibrations in high turbulence require the instrument under test (IUT) to be located directly downstream from the LDA. Fundamentally, blockage effects depend on the ratio of the air speed to the rate pressure waves propagate (*i.e.*, Mach number), and should be independent of the level of turbulence intensity. Nevertheless, we searched for a turbulence-dependence of the blockage, by installing an EPA-accepted multi-

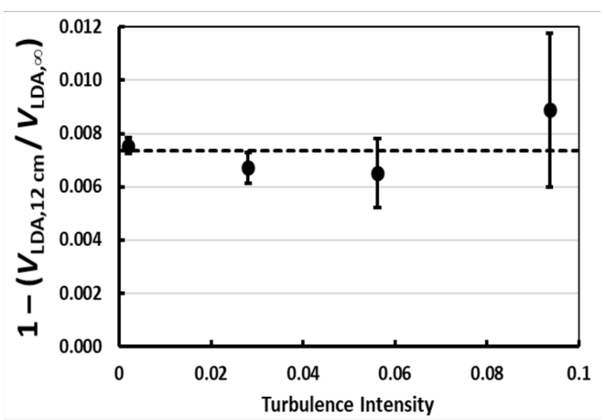

Figure 13: Turbulence dependence of blockage by an EPA-accepted multi-hole probe measured at 10 m/s. The uncertainty bars represent the standard deviation of the mean of 5 independent measurements. The dashed line represents the uncertainty-weighted mean of the plotted points. The data are consistent with the blockage being independent of the turbulence intensity.

hole probe just downstream of the LDA with an air speed of 10 m/s. The turbulence-generating grid was placed at three locations upstream of the test point (X = −1.06 m, − 2.00 m, or −3.56 m). As shown in Fig. 13, the blockage was independent of the turbulence, within the noise of the measurements.

8. Examples of Calibration Data

8.1 Multi-hole Differential Pressure Probe.

As part of a research program to make faster, more accurate, flue gas flow measurements in power plants [1], we acquired the data displayed in Fig. 14. The displayed data are a small fraction of the data that are needed to characterize the response of a 5-hole spherical probe for flue gas measurements. The full data set comprises the pressures measured at all 5 ports (relative to the static pressure) at pitch and yaw intervals of 2° at air speeds of 5 m/s, 10 m/s, 20 m/s, and 30 m/s and at 4 turbulence intensities. Routine acquisition of such large data sets for customer-provided probes is prohibitively expensive, even using a fully automated calibration system. One thrust of our research is to document methods of characterizing multi-hole spherical (and other) probes with much smaller data seta. This might be done by comparing the responses of each customer's probe to the corresponding responses of a nominally-identical "master" probe under only a few calibration conditions. Alternatively, the master probe could be replaced with a numerical and/or analytical model for the responses of an ideal probe.

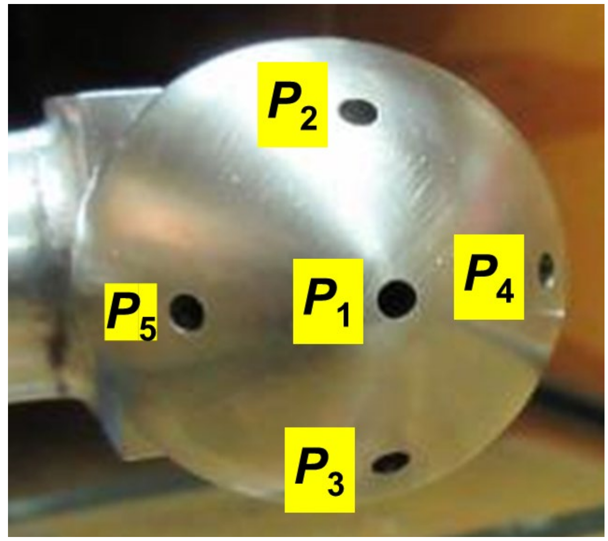

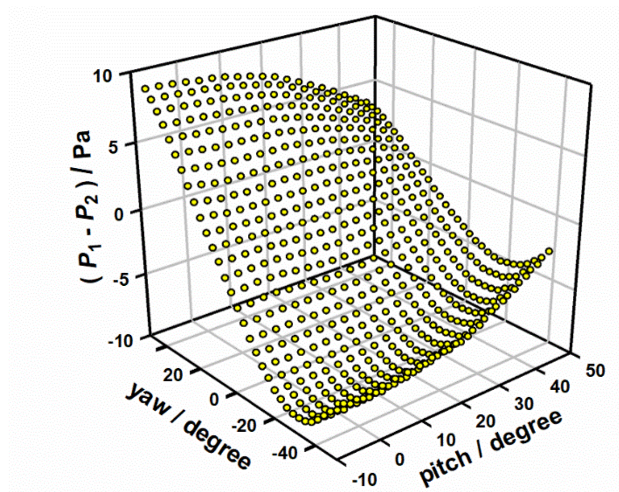

Figure 14. Top: 5-hole spherical probe with labels on pressure-sensing ports. Bottom: Pressure difference between ports P_1 and P_2 as a function of pitch and yaw angles. Data were taken at intervals of 2° at 5 m/s.

8.2 Vane anemometer

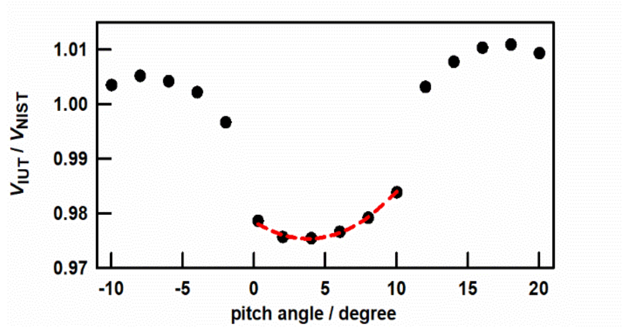

Figure 15. Pitch dependence of the calibration factor of a vane anemometer at an air speed near 10 m/s.

Some customers request that NIST calibrate an anemometer comprised of "vanes" or a "propeller" or an "impellor" that rotates about an axis parallel to the wind direction. Figure 15 is a sample of calibration data for a rotating vane anemometer with a protective cylindrical ring (or frame) surrounding the vanes. In Fig. 15, the zero on the pitch axis is arbitrary because no effort was made to align the anemometer's rotation axis with the axis of the wind tunnel. The plotted data show that the calibration factor V_{IUT}/V_{NIST} is insensitive to small changes of the pitch angle α at approximately $\alpha = 4°$. This angle was used to calibrate the IUT as a function of air speed. Figure 15 also shows that the calibration factor steps up when the pitch angle jumps decreases near $\alpha \approx -1°$ or increases near $\alpha \approx 12°$. We speculate that the frame begins to shadow the vanes at these angles.

8.3 Thermal anemometer

Figure 16 displays some of the calibration data for a thermal anemometer that was designed to be insensitive to its orientation with respect to the average wind speed. This anemometer's calibration factor was remarkably insensitive to the yaw angle; however, it did have an easily measured dependence on the pitch angle.

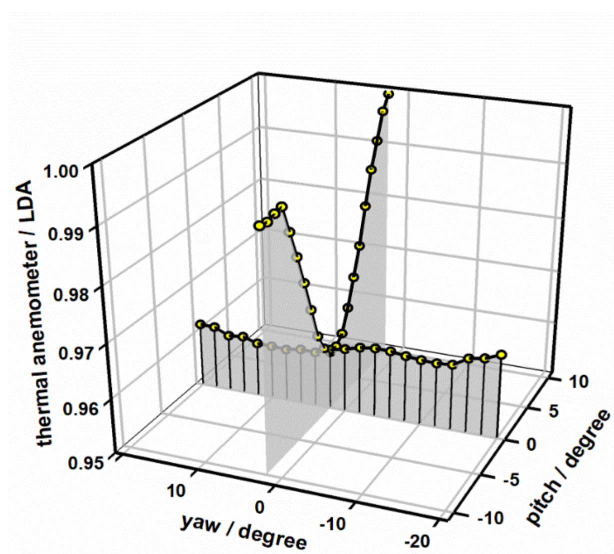

Figure 16. Calibration factor of a thermal anemometer at an air speed near 10 m/s.

9. Uncertainties

In Ref. [7] we discussed the uncertainties encountered when calibrating 3-D anemometers using NIST's one-dimensional LDA as a working standard. We tabulated uncertainty contributions from misalignment of the spinning disk with respect to the LDA, thermal expansion of the disk, the LDA's optical system, the clock of the burst spectrum analyzer, and of the LDA the clock, and the alignment of the IUT with respect to the LDA. All these uncertainty contributions were negligible in comparison with the ($k = 2$, expanded) 0.41 % uncertainty of the calibration factor of the LDA relative to the spinning disk standard in range 0.2 m/s to 10 m/s. As shown in Section 7 above, blockage effects can be significantly larger than the uncertainty of the LDA calibration factor; however, we correct for blockage. For moderately-sized probes (~2.5 cm diameter), the uncertainty of the blockage correction is negligible compared with other uncertainties.

Conclusion

We have updated NIST's wind tunnel so that it can perform blockage-corrected calibrations of anemometers as a function of the airspeed vector and turbulence intensity. The new vector and turbulence capabilities enable NIST to calibrate multi-hole differential-pressure probes that are used to quantify the flue gas flows from the smokestacks of coal-burning power plants. The calibration of the probes creates a chain of traceable measurements that starts with the SI and quantifies flue gas flows. The quantified flue gas flows are combined with with traceable flue gas composition measurements to obtain traceable values of pollution emissions. The international acceptance of this chain will support the equitable regulation of pollution emissions.

Acknowledgements

We thank Dr. John Wright of NIST for his continuing, enthusiastic support of this work. This research was partially funded by NIST's Greenhouse Gas and Climate Science Measurements Program administered by Dr. James Whetstone. Gregory Scace helped design and assemble the

3-D calibration rig. We thank Chris Crowley for his contributions to the laser Doppler anemometry. Joey Boyd has maintained the 3-D system.

References

[1] A. N. Johnson, I. I. Shinder, B. J. Filla, J. T. Boyd, R. Bryant, M. R. Moldover, T. D. Martz, and M. R. Gentry. "Faster, more accurate, stack-flow measurements." *Journal of the Air & Waste Management Association* **70**, no. 3 (2020): 283-291.

[2] Christopher J. Crowley, Iosif I. Shinder, and Michael R. Moldover, "The effect of turbulence on a of Multi-hole Pitot calibration," *Flow Meas. and Instrum*. **33**, 106-109 (2013).

[3] Steffan Johnson, Leader - Measurement Technology Group at US Environmental Protection Agency (EPA). Private email communication, 2014.

[4] https://www.bipm.org/kcdb/cmc/search?domain=PHYSICS&areaId=4&keywords=&specificPart.branch=15&specificPart.service=-1&specificPart.subService=-1&specificPart.individualService=384&_countries=1&publicDateFrom=&publicDateTo=&unit=-1&minValue=&maxValue=&minUncertainty=&maxUncertainty=

[5] Harald Müller, Isabelle Caré, Peter Lucas, Dietmar Pachinger, Noboru Kurihara, Cui Lishui, Chun-Min Su, Iosif Shinder, and Pier Giorgio Spazzini. "CCM. FF-K3. 2011: Final report for the CIPM key comparison of air speed, 0.5 m/s to 40 m/s." *Metrologia* 54, no. 1A (2017): 07013.

[6] Iosif I. Shinder, James R. Hall, and Michael R. Moldover. "Improved NIST Airspeed Calibration Facility", *Proc. Measurement Science Conf., Pasadena, CA, USA, March 22-26, 2010* ; NIST-formatted version is available at https://tsapps.nist.gov/publication/get_pdf.cfm?pub_id=904871

[7] Iosif I. Shinder, Iosif I., Christopher J. Crowley, B. James Filla, and Michael R. Moldover. "Improvements to NISTs air speed calibration service." *Flow Measurement and Instrumentation* **44** (2015): 19-26

[8] T.T. Yeh, J. M. Hall Airspeed Calibration Service. NIST Special Publication SP 250-79. (2007); NIST-formatted version is available at https://nvlpubs.nist.gov/nistpubs/Legacy/SP/nistspecialpublication250-79.pdf

[9] Iosif I. Shinder, Vladimir B. Khromchenko, Michael R. Moldover, "NIST's New 3D Airspeed Calibration Rig Addresses Turbulent Flow Measurement Challenges" *9th Intl Symp. on Fluid Flow Measurements, Arlington, VA, USA April 14-17, 2015*; NIST-formatted version is available at https://tsapps.nist.gov/publication/get_pdf.cfm?pub_id=918356

[10] Iosif I. Shinder, Michael R. Moldover, J. M. Hall, Mike Duncan, and Joe Keck. "Airspeed Calibration Services: Laser Doppler Anemometer Calibration and Its Uncertainty." In 8th Intl. Symp. on Fluid Flow Measurements. June 20-22, 2012, Colorado Springs, CO; NIST-formatted version is available at https://tsapps.nist.gov/publication/get_pdf.cfm?pub_id=911456

[11] Pier Giorgio Spazzini, Aline Piccato, Riccardo Malvano. "Metrological features of the linear low-speed anemometer calibration facility at INRIM". *Metrologia,*,**46**, (2009) pp. 109–118.

[12] Iosif I. Shinder, James R. Hall, and Michael R. Moldover, "Improved NIST Air Speed Calibration Facility", Proc. Measurement Sci. Conf., March 22-26, 2010, Pasadena, CA; NIST-formatted version is available at https://www.nist.gov/publications/improved-nist-airspeed-calibration-facility

[13] Osama Terra and Haitham M. Hussein. "Simple and accurate calibration system for Laser Doppler Velocimeters" *Optik*, **179**, (2019) 733-739.

[14] Simmons, L. F. G., and C. Salter. "Experimental investigation and analysis of the velocity variations in turbulent flow." *Proceedings of the Royal Society of London. Series A*, **145**, no. 854 (1934): 212-234.

[15] Thomas Kurian and Jens H M Fransson. "Grid-generated turbulence revisited", *Fluid Dyn. Res*. **41**, (2009) 021403.

[16] Giulio Vita, Hassan Hemida, Thomas Andrianne, Charalampos C. Baniotopoulos, "Generating atmospheric turbulence using passive grids in an expansion test section of a wind tunnel", *J. Wind Engineering & Industrial Aerodynamics* **178** (2018) 91–104

[17] Lianjie Liu, Liangliang Zhang, Bo Wu, Ben Chen, "Numerical and Experimental Studies on Grid-Generated Turbulence in Wind Tunnel" *J. Engineering Science and Technology Review* **10** (2017) 159-169

[18] Geoffrey Ingram Taylor, "Statistical theory of turbulence IV-diffusion in a turbulent air stream." *Proceedings of the Royal Society of London. Series A* **151**, no. 873 (1935): 465-478.

[19] Emmanuel Virota, Xavier Amandolesea, Pascal Hémona. *Unsteady forces induced by a flag in a wind tunnel*, 2013, 21ème Congrès Français de Mécanique, Bordeaux, 26 au 30 août.

[20] Sébastien Michelin, Stefan G. Llewellyn Smith, and Beverley J. Glover, "Vortex shedding model of a flapping flag", *J. Fluid Mech*, **617**, pp. 1-10 (2008).

[21] Jon V. Larssen and William J. Devenport, "On the generation of large-scale homogeneous turbulence", *Exp. Fluids* **50**, 1207–1223 (2011); Jon Vegard Larssen. "Large Scale Homogeneous Turbulence and Interactions with a Flat-Plate Cascade", Ph.D. thesis, Virginia Poly. Inst., Jan. 25th, 2005, Blacksburg, Virginia.